Journal of
Materials Chemistry C

ROYAL SOCIETY
OF CHEMISTRY

PAPER

View Article Online
View Journal | View Issue

Check for updates

Cite this: *J. Mater. Chem. C*, 2025, **13**, 6123

Deep-red to NIR solution-processed OLEDs of donor-decorated quinoxaline-based TADF aggregates†

Abhishek Kumar Gupta, *[ab] David B. Cordes, [a] Joydip De, [a] Alexandra M. Z. Slawin, [a] Stuart Warriner,[c] Ifor D. W. Samuel *[b] and Eli Zysman-Colman *[a]

Received 12th December 2024,
Accepted 21st January 2025

DOI: 10.1039/d4tc05238b

rsc.li/materials-c

We report the use of an extended π-conjugated electron-deficient "pyrazino[2,3-*g*]quinoxaline (**PQ**)" as a strong, planar acceptor in a donor–acceptor thermally activated delayed fluorescence (TADF) emitter design to achieve deep-red to NIR emission. A pair of multi-donor–acceptor (multi-D–A) emitters, **4DMAC-TPPQ** and **4PXZ-TPPQ**, using **PQ** as the strong acceptor and dimethylacridine (DMAC) and phenoxazine (PXZ) as strong donors, respectively, emit at 650 and 762 nm in toluene, which is significantly red-shifted in comparison to the parent compound **TPPQ** (λ_{PL} = 456 nm). Both compounds show aggregation-induced emission enhancement in THF:water mixtures. Both compounds exhibit TADF as doped films in 4,4′-bis(*N*-carbazolyl)-1,1′-biphenyl (CBP) and as neat films. The emission of the neat film is similar to that in toluene with λ_{PL} of 654 and 770 nm for **4DMAC-TPPQ** and **4PXZ-TPPQ**, respectively. Solution-processed organic light-emitting diodes (SP-OLEDs) of neat **4DMAC-TPPQ** showed electroluminescence (λ_{EL}) at 685 nm and an EQE_{max} of 0.3%, while the device with **4PXZ-TPPQ** emitted at an λ_{EL} of 780 nm and showed an EQE_{max} of 0.04%. The OLEDs with **4PXZ-TPPQ** showed the most red-shifted emission amongst those employing TADF emitters containing a quinoxaline-type acceptor.

Introduction

Materials that emit in the deep-red (650–700 nm) to near-infrared (NIR) (700–1400 nm) wavelength range are used in numerous applications, including biomedical imaging,[1–3] forensic science,[4,5] chemical sensors,[6,7] dyes in photovoltaic cells,[8] fibre optic telecommunications,[9–11] and electroluminescent devices.[12] Both transition metal complexes[11–13] and conjugated polymers[1,14] can be considered rather mature classes of red emitters; however, the development of purely organic emitters in the deep-red to NIR region is challenging because of three main issues. Firstly, red emitters are not as emissive as higher energy analogues due to the energy gap law, which states that radiative decay decreases and nonradiative decay accelerates as the emission wavelength shifts to the red. This is due to vibrational coupling between the excited state and the ground state.[15,16] Secondly, the use of large π-systems, particularly in terms of the electron acceptor in donor–acceptor emitter design, leads to aggregation-caused quenching (ACQ) of the emission.[16,17] Thirdly, most organic compounds are fluorescent and so only the electrogenerated singlet excitons are available to produce light in organic light emitting diodes (OLEDs), which limits the efficiency of these devices.[15,16]

One strategy to overcome these design limitations is to use thermally activated delayed fluorescence (TADF) emitters as these can harvest both singlet and dark triplet excitons to produce light in OLEDs.[18,19] To design an efficient NIR TADF emitter, the compound needs to possess a small singlet–triplet energy gap (ΔE_{ST}), which will enable a fast reverse intersystem (RISC) that should outcompete nonradiative decay pathways involving triplet excitons. This requires the use of rigid, planar and strong donor and acceptor motifs that are reasonably weakly coupled to each other to extend π-conjugation.[15,16] A second plausible strategy is to develop an emitter showing simultaneous TADF and aggregation-induced emission (AIE).[20,21] Our emitter design adheres to this latter paradigm. We envisioned having a strong acceptor motif (*i.e.*, $E_{LUMO} < -2.50$ eV); however, the choice of acceptor moieties

---

[a] *Organic Semiconductor Centre, EaStCHEM School of Chemistry, University of St Andrews, Fife KY16 9ST, UK. E-mail: eli.zysman-colman@st-andrews.ac.uk*
[b] *Organic Semiconductor Centre, SUPA. School of Physics and Astronomy, University of St Andrews, North Haugh, St Andrews, Fife KY16 9SS, UK*
[c] *School of Chemistry, University of Leeds, Woodhouse Lane, Leeds, UK*

† Electronic supplementary information (ESI) available: Compound characterization (^{1}H NMR, ^{13}C NMR, elemental analysis, and HRMS), SCXRD, photophysical studies, OLED data, and DFT calculations. Crystallographic information for **TPPQ**, **4DMAC-TPPQ** and **4PXZ-TPPQ**. CCDC 2406567–2406569. For ESI and crystallographic data in CIF or other electronic format see DOI: **https://doi.org/10.1039/d4tc05238b**

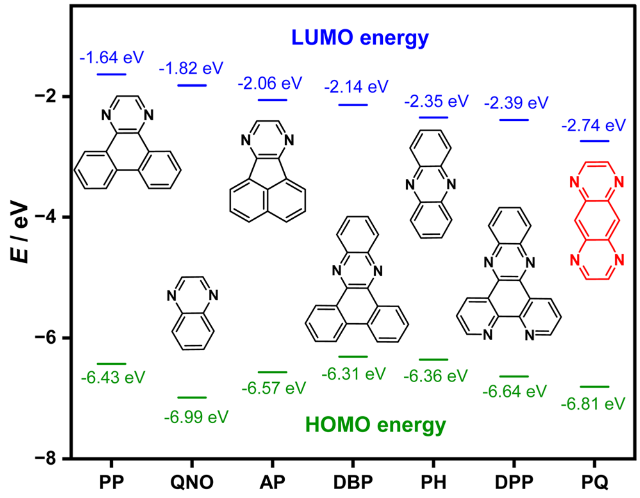

Fig. 1 Common pyrazine-based acceptor moieties and their corresponding highest occupied molecular orbital (HOMO) and lowest unoccupied molecular orbital (LUMO) energies, calculated at the PBE0/6-31G(d,p) level in a vacuum.

is somewhat limited, and most NIR TADF emitters ($\lambda_{PL} > 650$ nm) contain one of benzothiadiazole (BT),[22,23] pyridal[2,1,3]thiadiazole (PT),[24] naphtho[2,3-*c*][1,2,5]thiadiazole (NZP)[25] and pyrazine derivatives.[7,26,27] Out of these acceptor motifs, the most common pyrazine derivatives are phenanthropyrazine (PP), quinoxaline (QNO), acenaphthopyrazine (AP), dibenzophenazine (DBP), phenazine (PH), and dipyridophenazine (DPP), and their acceptor strengths are shown in Fig. 1.

With the goal of pushing the emission further into the NIR, our acceptor design contains a dipyrazine embedded within an extended π-conjugative framework in the form of a pyrazinequinoxaline (**PQ**). This motif can also be thought of as a fused tetraazaanthracene. Consequently, the presence of four nitrogen atoms makes the system quite electron deficient, reflected in a LUMO energy of −2.74 eV (Fig. 1). Because of their strong accepting nature, **PQ**-based materials have been explored as fluorescent sensors,[28] as motifs in organic liquid-crystalline semiconductors,[29–31] and as components in OLEDs[23] and organic photovoltaics (OPVs).[29] Chen *et al.* reported an AIE active fluorescent donor–acceptor system based on **PQ** derivatives that exhibited green and red emission from their aggregates, and utilized these in bio-imaging applications.[32] Vishwakarma *et al.* reported a **PQ** based columnar liquid crystalline material (**PQ10**) and its use as a fluorescent emitter for green OLEDs.[30] Due to the impressive hole transporting mobility of **PQ10**, it was also used as a hole transporting material for photovoltaic applications.[29]

In our bid to design NIR emitters, we decorated the **PQ** moiety with four electron-donating groups, either dimethylacridane (DMAC) or phenoxazine (PXZ),[33–35] each separated by a phenylene bridge to the central **PQ** acceptor. We cross-compare the optoelectronic properties of **4DMAC-TPPQ**, and **4PXZ-TPPQ** with that of the electron-acceptor **TPPQ** (Scheme 1), including assessing whether each of these compounds shows aggregation-induced emission enhancement (AIE). **TPPQ** emits in the blue (λ_{PL} = 456 nm) in toluene, while **4DMAC-TPPQ** and **4PXZ-TPPQ** emit at 650 and 762 nm, respectively (Fig. 4). Their corresponding ΔE_{ST} values, obtained in glassy 2-MeTHF at 77 K, are 0.97, 0.41 and 0.24 eV. All these compounds show AIE in THF:H_2O mixtures; indeed, upon increasing the water fraction in THF solution, the blue PL band peaking at 490 nm intensified,

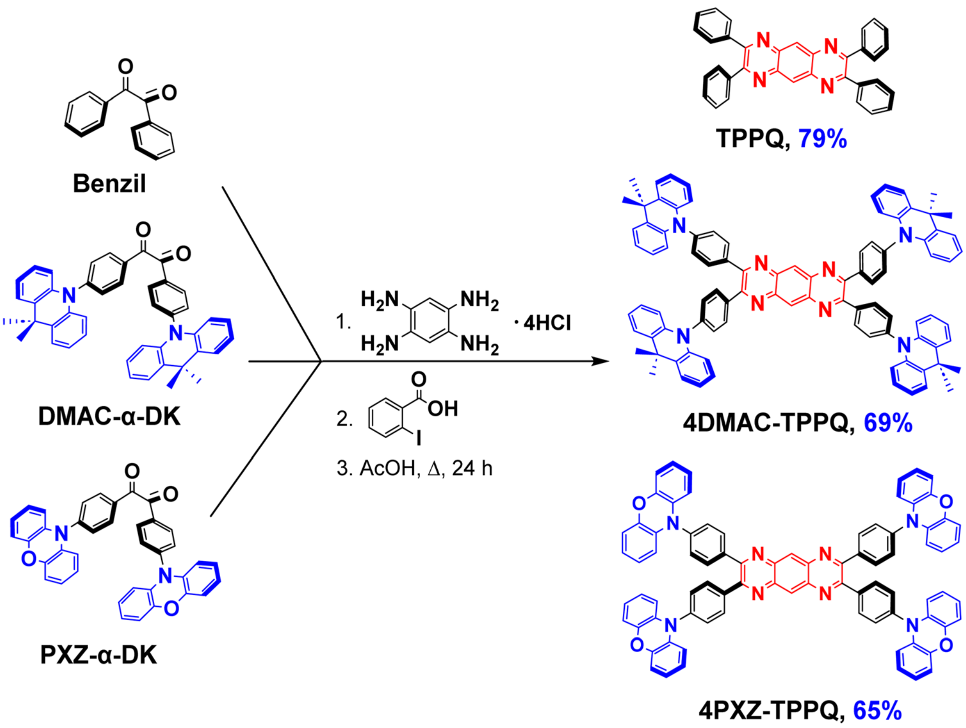

Scheme 1 Synthetic scheme of **TPPQ**, **4DMAC-TPPQ**, and **4PXZ-TPPQ**.

which is associated with locally-excited emissions from **TPPQ**. Additionally, for **4DMAC-TPPQ**, there is the appearance of a deep-red band at 650 nm and for **4PXZ-TPPQ** a band at 790 nm emerges, both of which are associated with aggregate formation (Fig. 5). **4DMAC-TPPQ** shows emission from 627 to 654 nm and **4PXZ-TPPQ** shows emission from 682 to 770 nm by varying the doping concentration from 5 to 50 wt% in CBP and in neat film with lowering the ΔE_{ST} to 0.29 and 0.04 eV, respectively (Fig. S34, ESI† and Table 2). Finally, we fabricated doped (in CBP) and neat film solution-processed OLEDs (SP-OLEDs) of **4DMAC-TPPQ** and **4PXZ-TPPQ**. The neat film SP-OLEDs with **4DMAC-TPPQ** emitted with an electroluminescence maximum, λ_{EL}, of 685 nm, while neat film SP-OLEDs with **4PXZ-TPPQ** emitted at an λ_{EL} of 780 nm. Notably, the PL spectrum of **4PXZ-TPPQ** and the EL spectrum of the OLED with this emitter were the most red-shifted among those of the 19 other TADF emitters containing a quinoxaline-type acceptor (Fig. S43 and Table S11, ESI†). Remarkably, we also enabled the TADF phenomena in **TPPQ** containing emitters, which was absent in previously reported compounds containing the **TPPQ** moiety.[30,32]

Results and discussion

The α-diketone derivatives of benzil-containing 9,9-dimethyl-9,10-dihydroacridine (**DMAC-α-DK**) and 10*H*-phenoxazine (**PXZ-α-DK**) moieties were synthesized through a palladium-catalysed Buchwald–Hartwig cross-coupling between 4,4′-dibromobenzil and DMAC or PXZ according to our previously reported procedure.[34] Benzil, **DMAC-α-DK** and **PXZ-α-DK** were condensed with 1,2,4,5-tetraaminobenzene tetrahydrochloride to afford pyrazinyl[2,3-*g*]quinoxaline derivatives **TPPQ**, **4DMAC-TPPQ** and **4PXZ-TPPQ**, respectively, in good yield (Scheme 1). Their identity and purity were determined by a combination of ^{1}H and ^{13}C NMR spectroscopy, high-pressure liquid chromatography (HPLC), high-resolution mass spectrometry (HRMS), elemental analysis, and single crystal X-ray diffraction (SC XRD) (Fig. 1 and Fig. S1–S15, ESI†). The decomposition temperature (T_d), defined as the 5% weight loss of the material, is 356 °C for **TPPQ**, 445 °C for **4DMAC-TPPQ** and 495 °C for **4PXZ-TPPQ** (Fig. S16, ESI†). Thus, all three compounds show high thermal stability. DSC measurements reveal very high glass transition temperatures (T_g) of 292 °C, 432 °C, and 450 °C for **TPPQ**, **4DMAC-TPPQ** and **4PXZ-TPPQ**, respectively.

Single crystals of **TPPQ**, **4DMAC-TPPQ** and **4PXZ-TPPQ** suitable for X-ray diffraction were grown by slow evaporation from either a mixture of dichloromethane and hexane, or chloroform and THF. The structures of **TPPQ**, **4DMAC-TPPQ** and **4PXZ-TPPQ** are found in the centrosymmetric space groups $P2_1/c$ (**TPPQ**) and $P2_1/n$ (both other structures). For **TPPQ** and **4DMAC-TPPQ** the asymmetric unit contains one half of an emitter molecule, as well as one or two molecules of dichloromethane, respectively, while the asymmetric unit of the structure of **4PXZ-TPPQ** contains a complete emitter molecule. The four phenyl rings attached to the central core of **PQ** in **TPPQ** are somewhat twisted, with dihedral angles between phenyl rings and the planes of **PQ** of 34.32(14) and 57.55(14)° (Fig. 2). The corresponding dihedral angles are 34.74(16) and 49.47(6)° in **4DMAC-TPPQ**, and 47.81(12), 47.84(12), 48.60(5) and 58.02(15)° in **4PXZ-TPPQ**, while the dihedral angles between the bridging phenylene rings and the mean plane of the central six-membered heterocycle of the donor moieties show more twist at 69.95(6) and 78.23(7)° for **4DMAC-TPPQ**, and 59.27(13), 62.24(13), 68.40(6) and 73.17(18)° for **4PXZ-TPPQ** (Fig. 2a). This leads to the donor and acceptor groups being closer to co-planar in **4PXZ-TPPQ** than in **4DMAC-TPPQ**, the angles between the **PQ** plane and the central ring of the DMAC are 29.54(6) and 33.37(6)° in **4DMAC-TPPQ**, while in **4PXZ-TPPQ** the equivalent angles are decreased to 12.12(14), 15.25(13), 16.26(16) and 20.8(4)°. The **DMAC** groups show bowed conformations, with angles between phenyl ring planes of 23.23(8) and 33.19(8)°, while in **4PXZ-TPPQ** three of the **PXZ** donor groups show slightly bowed conformations (angle between phenyl ring planes 14.1(6), 14.68(16), 15.87(15)°) while one is closer to planar (angle between phenyl ring planes 5.8(2)°). The structure of **TPPQ** is a DCM solvate form of the previously reported structure, showing a very similar molecular conformation, but with molecules packed in a herringbone fashion (Fig. S17a, ESI†), rather than the previously encountered parallel sheet structure.[32] There are two sets of C–H···π intermolecular interactions between adjacent **TPPQ** molecules. One of these arises between a peripheral phenyl hydrogen and the central ring of the **PQ** group (H···centroid distance of 2.81 Å, C···centroid distance of 3.472(4) Å), which leads to chains of **TPPQ** molecules along the [0 1 0] axis. These are linked into two-dimensional sheets in the (1 0 0) plane (Fig. 2b) by the second set of C–H···π interactions, arising between symmetry-related phenyl rings (H···centroid distance of 2.94 Å, C···centroid distance of 3.608(5) Å). The crystal structure of **4DMAC-TPPQ** shows a combination of weak π···π and C–H···π intermolecular interactions, leading to a brickwork packing (Fig. S17b, ESI†). There are two sets of C–H···π intermolecular interactions between adjacent molecules. One of these arises between a bridging phenyl hydrogen and a phenyl of a **DMAC** group (H···centroid distance of 3.00 Å, C···centroid distance of 3.729(2) Å), the second between methyl hydrogen and a pyrazine ring of the **PQ** group (H···centroid distance of 2.99 Å, C···centroid distance of 3.537(3) Å). The CH···π interactions result in the formation of sheets in the (−1 0 1) plane (Fig. 2b), which are further supported by the π···π interactions between one pyrazine ring and another phenyl of a **DMAC** (centroid···centroid distance 3.8477(11)). In the structure of **4PXZ-TPPQ**, molecules show undulating layered packing, with channels for solvent (Fig. S17c, ESI†). This complex shows a more significant and more complex arrangement of supramolecular interactions. This comprises two-dimensional sheets in the (0 0 1) plane, built up of a combination of nine sets of interactions (Fig. 2b). These include two sets of π···π interactions from the central benzene ring of the **PQ** group to two peripheral phenyls, forming a three-layered π-stack (centroid···centroid distances of 3.570(2) and 3.616(2) Å), four sets of weak hydrogen bonds between four different aromatic CH groups of the bridging phenyls and two pyrazine nitrogen and two oxygen atoms of the **PXZ** groups (H···N distances of 2.47 and 2.60 Å, corresponding C···N

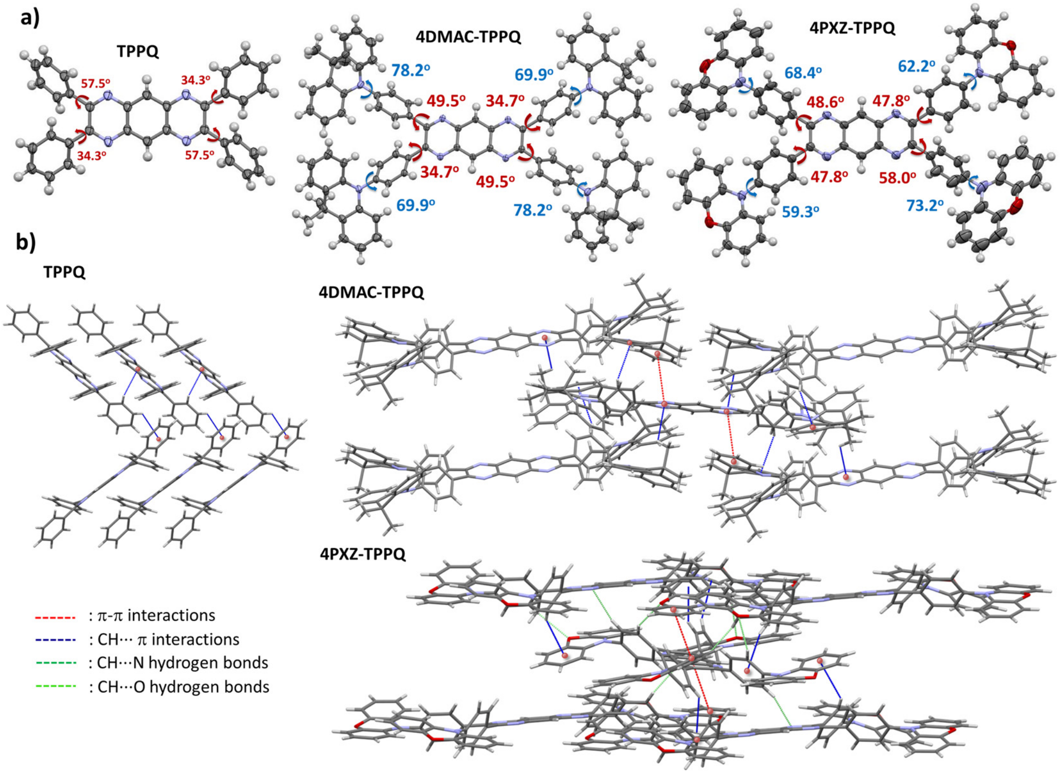

Fig. 2 (a) Thermal ellipsoid plots of the crystal structures with dihedral angles between the bridging phenylene ring and both donor and acceptor moieties of **TPPQ**, **4DMAC-TPPQ** and **4PXZ-TPPQ**. Ellipsoids are shown at the 50% probability level. (b) Views of the structure of **TPPQ**, **4DMAC-TPPQ** and **4PXZ-TPPQ** showing the intermolecular interactions leading to the formation of two-dimensional sheets. Solvent molecules and minor components of disorder are omitted.

distances of 3.302(4) and 3.439(4) Å; H···O distances of 2.59 Å, with C···O distances of 3.414(5) and 3.448(6) Å), and three sets of CH···π interactions between three different aromatic CH groups of the bridging phenyls and one other bridging phenyl and two proximal phenyl groups of **PXZ** (H···centroid distances of 2.93 to 3.00 Å, C···centroid distances of 3.753(4) to 3.901(3) Å). These sheets are in turn weakly connected into a three-dimensional supramolecular structure *via* two further sets of dimer-forming π···π interactions between two phenyl groups of **PXZ** and their symmetry-related neighbours (centroid···centroid distances of 3.726(10) and 3.947(3) Å) at the close points of approach of the undulations (Fig. S17c, ESI†).

Theoretical studies

Density functional theory (DFT) and time-dependent DFT calculations within the Tamm–Dancoff approximation (TDA-DFT) were performed to provide insight into the geometries and energies of the ground and the excited states of **TPPQ**, **4DMAC-TPPQ** and **4PXZ-TPPQ**. The ground-state geometries were optimized at the PBE0/6-31G(d,p) level of theory in the gas phase starting from the geometries obtained from the single crystal structures (Fig. 3). The central **PQ** moiety is almost planar in all three molecules, with dihedral angles between the planes of both pyrazine nitrogen in symmetrical pyrazine rings of 3.88° in **TPPQ**, 3.74° in **4DMAC-TPPQ** and 3.79° in **4PXZ-TPPQ**. In **TPPQ**, all four phenyl rings are equally twisted to the **PQ** with an angle of 39.68°, whereas the dihedral angles between the phenylene rings and **PQ** in **4DMAC-TPPQ** are 41.97 and 45.88° and in **4PXZ-TPPQ** are 43.31 and 43.49°. In **4DMAC-TPPQ**, the DMAC moieties are strongly twisted with respect to the phenylene bridge (76.56 and 76.24°), while in **4PXZ-TPPQ** the PXZ moieties are slightly less twisted (70.64 and 71.37°, Fig. S18, ESI†). Moreover, the DMAC units retained their puckered/bowed conformations, with dihedral angles between the phenyl ring planes of 31.72° and 28.96°. Their conformation is well matched with that in the corresponding crystal structure; however, the PXZ units exhibited more planar conformations than seen in the crystal structure, with dihedral angles between their phenyl ring planes of 2.07° and 2.32°. The electron density of the highly occupied molecular orbital (HOMO) is delocalized over the whole **TPPQ** molecule, while the lowest unoccupied molecular orbital (LUMO) is somewhat more concentrated on the pyrazino[2,3-*g*]quinoxaline. The HOMO/LUMO levels are −6.23/−2.56 eV. A similar electron density distribution pattern of the orbitals of **TPPQ** has been previously reported, though those calculations diverge from those reported here as they included a THF environment and were carried out at the lower B3LYP/6-31G(d) level.[32] However, the literature calculated HOMO level was slightly shallower at −6.15 eV, whilst the LUMO level was deeper at −2.80 eV. Both **4DMAC-TPPQ** and **4PXZ-TPPQ** exhibit a similar pattern in the distribution of the electron densities to **TPPQ**, with the HOMO distributed across

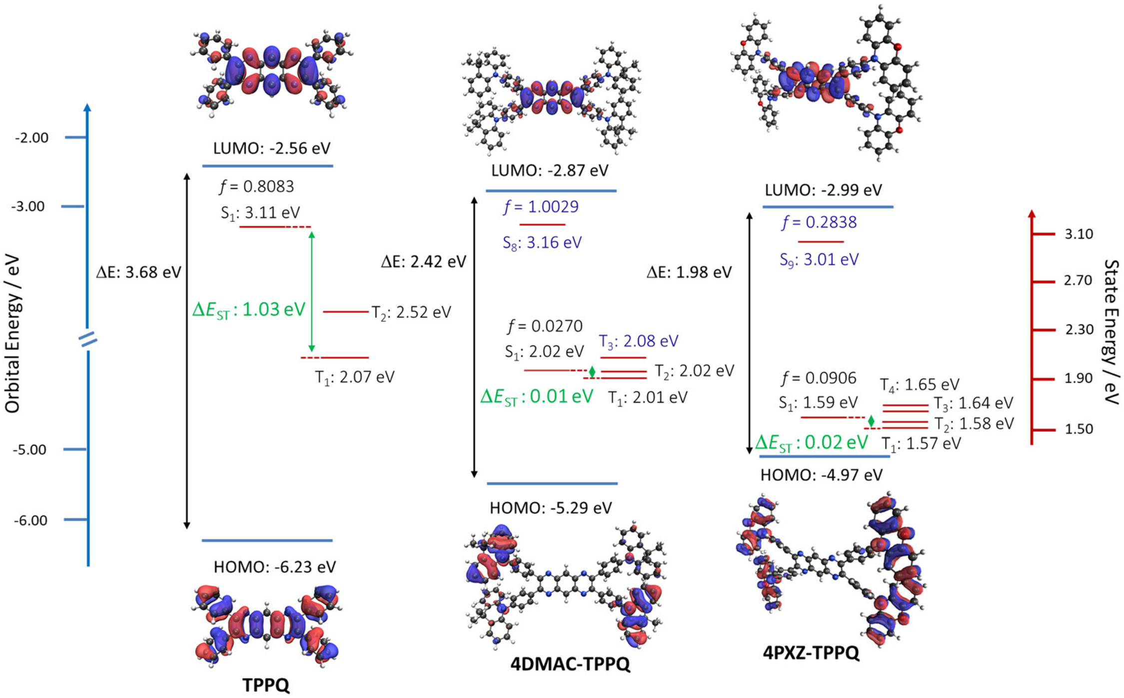

Fig. 3 The HOMO and LUMO distributions (isovalue = 0.02) of **TPPQ**, **4DMAC-TPPQ** and **4PXZ-TPPQ**, together with the transition energies for the relevant lowest singlet and triplet states calculated at the PBE0/6-31G(d,p) level in the gas phase.

the four donors and the LUMO localized mainly on the **PQ** acceptor (Fig. 3). Consequently, the HOMO levels are shallower compared to **TPPQ** at −5.29 eV for **4DMAC-TPPQ** and −4.79 eV for **4PXZ-TPPQ**, in line with their increasing donor strength, and the LUMO levels are stabilized compared to **TPPQ**, at −2.87 eV for **4DMAC-TPPQ** and −2.99 eV for **4PXZ-TPPQ**. The HOMO–LUMO gap, $\Delta E_{\text{HOMO-LUMO}}$, thus decreases from 3.67 eV for **TPPQ** to 2.42 eV for **4DMAC-TPPQ** and 1.80 eV for **4PXZ-TPPQ**.

The excited-state properties were calculated using time-dependent density functional theory (TD-DFT) within the Tamm–Dancoff approximation (TDA-DFT) based on the optimized ground-state geometries. The oscillator strength, *f*, of the $S_0 \rightarrow S_1$ transition in **TPPQ** is high at 0.808, indicating a significant overlap of the electron density between the HOMO and LUMO (Fig. S19 and Table S3, ESI†). However, the *f* for the $S_0 \rightarrow S_1$ transition of **4DMAC-TPPQ** and **4PXZ-TPPQ** is much lower at 0.027 and 0.091, respectively, reflecting the charge-transfer (CT) nature of this transition in these two compounds (Fig. S19 and Tables S4, S5, ESI†). The S_1 energy of **TPPQ** is 3.11 eV, while those of **4DMAC-TPPQ** (2.03 eV) and **4PXZ-TPPQ** (1.59 eV) are significantly stabilized (Fig. 3 and Tables S2–S5, ESI†). This trend in S_1 energies mirrors the trend in the HOMO–LUMO gaps. The T_1 state of **TPPQ**, mainly located on the pyrazine rings, is 2.07 eV and, like the S_1 state, also has a locally-excited (LE) character. The T_1 state of **4DMAC-TPPQ** at 2.01 eV is slightly lower in energy, while the T_1 state of **4PXZ-TPPQ** at 1.57 eV is significantly stabilized, reflecting their CT character (Fig. 3 and Table S6, ESI†). The corresponding calculated singlet–triplet energy gaps (ΔE_{ST}) of **4DMAC-TPPQ** (0.01 eV) and **4PXZ-TPPQ** (0.02 eV) are much smaller than that of **TPPQ** (1.03 eV) (Fig. 3). There are multiple high-lying triplet states in **4DMAC-TPPQ** and **4PXZ-TPPQ**, some of which have a different orbital type to S_1, and may participate in the TADF process in these two compounds (Fig. 3 and Table S7, ESI†). Additionally, at an excited T_1 geometry, there is a decrease in the S_1–T_1 spin–orbit coupling matrix element (SOCME) from 3.99 cm^{-1} in **TPPQ** to 0.01 cm^{-1} in **4DMAC-TPPQ** and 0.02 cm^{-1} in **4PXZ-TPPQ** (Table S6, ESI†). It should be noted that the SOCME of S_1–T_n ($n > 1$) in **4DMAC-TPPQ** ($\langle S_1|H_{\text{SO}}|T_3\rangle$ 0.03 cm^{-1}) and in **4PXZ-TPPQ** ($\langle S_1|H_{\text{SO}}|T_3\rangle$ is 0.06 cm^{-1}) is larger because of the large changes in orbital character between these two states (Table S6, ESI†). All these studies support a RISC process could proceed *via* the T_3 to S_1 in **4DMAC-TPPQ** and the T_3 to S_1 in **4PXZ-TPPQ** as T_3 lies just 0.06 eV above S_1 for **4DMAC-TPPQ** and 0.05 eV above S_1 for **4PXZ-TPPQ**, so is readily accessible because of their relatively large SOCME between these states.

Electrochemistry

Cyclic voltammetry (CV) and differential pulse voltammetry (DPV) measurements were used to infer the HOMO/LUMO levels of **TPPQ**, **4DMAC-TPPQ**, and **4PXZ-TPPQ** in DCM. The voltammograms are shown in Fig. 4a and the data are summarized in Table 1. As expected, there is no observable oxidation wave for **TPPQ**, while there are two 1-electron reversible reduction waves at $E_{\text{red1}} = -1.00$ V and $E_{\text{red2}} = -1.49$ V *vs.* SCE in DCM, in line with the literature-reported electrochemistry.[32] The corresponding orbital energies are LUMO = −3.34 eV and LUMO+1 = −2.85 eV. **4DMAC-TPPQ** possesses a quasi-reversible oxidation wave at E_{ox} at 1.00 V *vs.* SCE, which is assigned to the

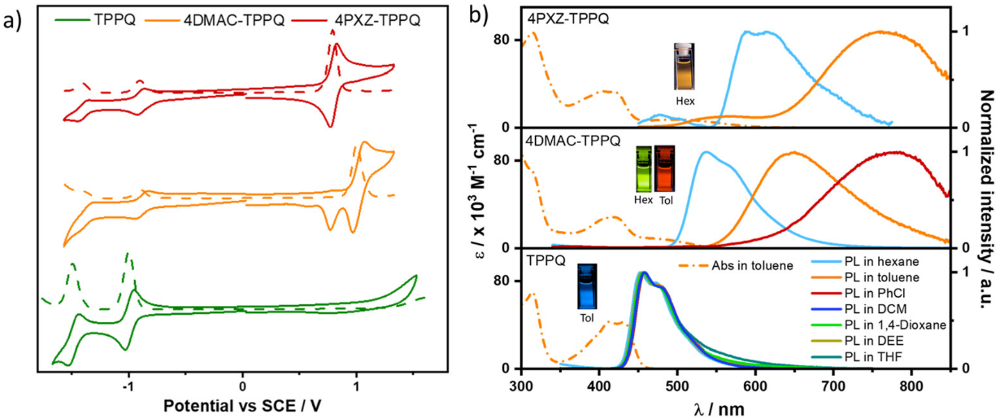

Fig. 4 (a) Cyclic and differential pulse voltammograms of **TPPQ**, **4DMAC-TPPQ** and **4PXZ-TPPQ** in degassed DCM (scan rate = 100 mV s^{-1}). (b) Absorption in toluene and photoluminescence spectra of 5 × 10^{-5} M **TPPQ**, **4DMAC-TPPQ** and **4PXZ-TPPQ** in various solvents (λ_{exc} = 315 nm).

Table 1 Electrochemical data and HOMO–LUMO levels for **TPPQ**, **4DMAC-TPPQ** and **4PXZ-TPPQ**

Emitters	E_{ox}[a]/V	E_{red}[a]/V	HOMO[b]/eV	LUMO[b]/eV	E_{opt}/eV
TPPQ	—	−1.00	−6.12[c]	−3.34	2.78
4DMAC-TPPQ	1.00	−0.89	−5.34	−3.45	2.32
4PXZ-TPPQ	0.79	−0.90	−5.13	−3.44	2.08

[a] E_{ox} and E_{red} are anodic and cathodic peak potentials, respectively, obtained from DPV using F_c/F_c^+ as the internal reference and referenced *versus* SCE (0.46 V *vs.* SCE) in DCM with 0.1 M [$^nBu_4N$]PF_6 as the supporting electrolyte.[36] [b] $E_{HOMO/LUMO}$ = $-(E^{ox}/E^{red} + 4.8)$ eV,[37] where E^{ox} is the anodic peak potential and E^{red} is the cathodic peak potential calculated from DPV relative to F_c/F_c^+. [c] $E_{HOMO} = |E_{LUMO} - E_{opt}|$ where E_{opt} is the optical band gap obtained from the intersection of the normalized absorption and emission spectra in toluene (Fig. S25, ESI).

oxidation of the DMAC donor moieties as this value aligns with the previously reported E_{ox} of 1.04 V for the DMAC-containing compound **DMAC-α-DK**.[34] The reversible oxidation wave of **4PXZ-TPPQ** is shifted cathodically at 0.79 V *vs.* SCE and is attributed to the oxidation of the **PXZ** donor moieties; indeed, the E_{ox} of **4PXZ-TPPQ** is similar to that of a related PXZ-containing compound, PXZPDO (E_{ox} = 0.83 V).[33] The HOMO levels thus are −5.34 and −5.13 eV for **4DMAC-TPPQ** and **4PXZ-TPPQ**, respectively, which are in line with the values and trends calculated using DFT (*vide supra*). The reduction waves are assigned to the reduction of the **TPPQ** acceptor, at around −1.00 V *vs.* SCE for both emitters. The corresponding LUMO energy levels are very similar, at −3.45 and −3.44 eV for **4DMAC-TPPQ** and **4PXZ-TPPQ**, respectively; the LUMO+1 for **4DMAC-TPPQ** is −2.94 eV and for **PXZ-TPPQ** is −2.93 eV, quite close to the LUMO+1 energy of **TPPQ**. The estimated HOMO level of **TPPQ** is inferred to be −6.12 eV from the difference between the LUMO level and the optical gap (ΔE_g = 2.78 eV) of **TPPQ** (Table 1). The HOMO–LUMO energy gap of **TPPQ** (2.78 eV) is much larger than that of **4DMAC-TPPQ** (1.89 eV) and **4PXZ-TPPQ** (1.69 eV).

Solution-state photophysical studies

The photophysical properties of all three molecules were first studied in toluene solution (Fig. 4b and Table S8, ESI†). There are three distinct absorption bands in the UV-vis absorption spectra of **4DMAC-TPPQ** and **4PXZ-TPPQ**, while there are only two bands in the spectrum of **TPPQ**. The strong absorption band at 314 nm present in all three spectra corresponds to a LE π–π* transition of the **TPPQ** moiety (ε = 69.9 × 10^3 M^{-1} cm^{-1} for **TPPQ**, ε = 70.5 × 10^3 M^{-1} cm^{-1} for **4DMAC-TPPQ** and ε = 86.9 × 10^3 M^{-1} cm^{-1} for **4PXZ-TPPQ**); the intensity of this band is influenced by the decoration about the acceptor (Fig. 4b). The absorption band located at 413 nm (ε = 42.9 × 10^3 M^{-1} cm^{-1} for **TPPQ**, ε = 28.2 × 10^3 M^{-1} cm^{-1} for **4DMAC-TPPQ** and ε = 32.9 × 10^3 M^{-1} cm^{-1} for **4PXZ-TPPQ**) is of mixed LE/CT character, based on an analysis of the TD-DFT calculations, where the LE transition is centred on the acceptor and the CT transition occurs from the phenylene groups to the **PQ** (Fig. S19, ESI†). The weakly absorptive CT band of **4PXZ-TPPQ** (ε = 7.57 × 10^3 M^{-1} cm^{-1} at λ_{abs} = 506 nm) and **4DMAC-TPPQ** (ε = 8.75 × 10^3 M^{-1} cm^{-1} at λ_{abs} = 475 nm) reflects the poor orbital overlap between the donor and the **PQ** acceptor (Fig. 4); notably, the red-shifted band in **4PXZ-TPPQ** is consistent with its smaller HOMO–LUMO gap compared to that of **4DMAC-TPPQ**, as observed in the electrochemistry study. The photoluminescence (PL) of **TPPQ** does not change as a function of solvent, with a peak maximum, λ_{PL}, of around 456 nm, and a shoulder band at around 476 nm (Fig. 4b). This, coupled with the reasonably narrow FWHM (56 nm), indicates that the emission emanates from a LE state. In contrast, **4DMAC-TPPQ** and **4PXZ-TPPQ** show unstructured and broad emission that is sensitive to solvent polarity and thus is assigned to originating from a CT state. In toluene, **4DMAC-TPPQ** emits at a λ_{PL} of 650 nm, while **4PXZ-TPPQ** emits at a λ_{PL} of 762 nm (Fig. 4b and Table S8, ESI†).

Unexpectedly, we observed that **TPPQ** showed photochromic behaviour in ethereal solvents. On exposure to UV light (365 nm) at room temperature in THF solution, over 6 minutes the blue band at 456 nm decreased in intensity while a broad, green band at 556 nm appeared, with a corresponding iso-emissive point at 504 nm (Fig. S21, ESI†). At 77 K in glassy 2-MeTHF, there is no appearance of the green emission band and only the narrow blue emission band at 448 nm is observed (Fig. S22, ESI†). There were no changes in the ^{1}H NMR spectrum of **TPPQ** in THF-d^8 before and after exposure to UV light (Fig. S23, ESI†), which confirms that that there is no photodegradation of **TPPQ**. From these experiments, the appearance of the new green emission band at 556 nm in **TPPQ** is attributed to excimer formation. To corroborate these conclusions, we modelled a **TPPQ** dimer, which has a more stable S_1 energy of 2.86 eV compared to the S_1 energy of the **TPPQ** monomer of 3.11 eV (Fig. S20, ESI†). Both **4DMAC-TPPQ** and **4PXZ-TPPQ** also showed a similar but weak photochromic behaviour in ethereal solvents (Fig. S24, ESI†).

The photoluminescence quantum yield (Φ_{PL}) in degassed toluene of **4DMAC-TPPQ** is 13.7%, higher than those of **TPPQ** (2.1%) and **4PXZ-TPPQ** (0.8%). Upon exposure to air, the Φ_{PL} for **TPPQ**, **4DMAC-TPPQ** and **4PXZ-TPPQ** decreases to 1.9, 7.3, and 0.6%, respectively. The PL decays of the three emitters in toluene under degassed and aerated conditions are shown in Fig. S26 (ESI†). There is only a single decay component observed for all three compounds, with lifetimes, τ_{PL}, of 7.9 ns for **TPPQ**, 20.2 ns for **4DMAC-TPPQ** and 1.98 ns for **4PXZ-TPPQ**.

The steady-state PL and phosphorescence spectra of **4DMAC-TPPQ** and **4PXZ-TPPQ** in 2-MeTHF glass at 77 K were measured to ascertain the S_1 and T_1 levels from their respective onsets; the S_1 and T_1 levels of **TPPQ** were measured in methylcyclohexane (MCH) at 77 K to mitigate against possible photochromism in 2-MeTHF (Fig. S27, ESI†). In glassy MCH, the λ_{PL} of **TPPQ** is around 456 nm, while the delayed emission spectrum of **TPPQ**, attributed to phosphorescence, peaks at 766 nm. Notably, there is a weak residual prompt emission at around 460 nm. The corresponding S_1 and T_1 energies are 2.82 and 1.85 eV, and thus the ΔE_{ST} is 0.97 eV. The S_1 and T_1 energies of **4DMAC-TPPQ** are 2.26 and 1.85 eV, while for **4PXZ-TPPQ** they are 2.08 and 1.84 eV (Fig. S27, ESI†). Thus, in these two compounds the S_1 energies follow the trend calculated by DFT and the observed HOMO–LUMO gaps determined by electrochemistry, while the T_1 energies, which are effectively the same as that of **TPPQ**, reflect the same ^{3}LE state. The corresponding ΔE_{ST} values of **4DMAC-TPPQ** and **4PXZ-TPPQ** are 0.41 and 0.24 eV, respectively.

Aggregation-induced emission (AIE)

TPPQ has previously been reported as an AIE-active moiety.[32] Aware of this, we assessed whether **4DMAC-TPPQ** and **4PXZ-TPPQ** would also show AIE and thus explored their PL spectra in THF/H_2O mixtures (Fig. 5a–c). Firstly, we re-confirmed the AIE behaviour of **TPPQ** in THF/H_2O mixtures. The emission peaking at 456 and 476 nm of **TPPQ** in THF slightly red-shifts and increases in intensity by 1.8-fold upon increasing the water fraction (f_w) to 60% (Fig. 5c and Fig. S28a, ESI†). On further increasing the f_w beyond 80%, the emission intensity then decreases and red-shifts further to 492 nm. We confirmed the formation of crystalline aggregates by powder XRD (Fig. S29, ESI†). Comparison of the powder XRD patterns to those simulated from the SC XRD data indicates structural differences, particularly in the cases of **TPPQ** and **4DMAC-TPPQ**, likely arising from the influence of solvent and its ordering on the structures. However, in the case of **4PXZ-TPPQ**, which lacks ordered solvent in its structure, a stronger similarity is seen between calculated and determined PXRD patterns. In comparison to **TPPQ**, **4DMAC-TPPQ** shows very weak emission at λ_{PL} of 568 nm, while **4PXZ-TPPQ** does not show any emission in THF, which points to non-radiative decay being significant in THF. Upon increasing f_w to 80%, the λ_{PL} of **4DMAC-TPPQ** red-shifts to 656 nm and becomes as much as 20-fold more intense (Fig. 5b and Fig. S28b, ESI†). Upon increasing the f_w from 80 to 95%, the emission intensity slightly decreases and further red-shifts to 690 nm. In the case of **4PXZ-TPPQ**, upon increasing the f_w to 40%, a new emission band at λ_{PL} of 790 nm appears, the intensity of which increases 23-fold at f_w = 80% (Fig. 5c and Fig. S28c, ESI†). When the f_w > 80%, the PL intensity decreases and slightly blue-shifts to 770 nm. In both molecules, the observed AIE is attributed to the formation of aggregates, as found in their crystal structures. The red-shifted emission observed from the aggregates formed in the 80% H_2O/THF mixture in both molecules likely occurs because of stronger intermolecular interactions between adjacent donor and acceptor moieties that modulate the energy of intermolecular CT states. To understand the emissive behaviour of the

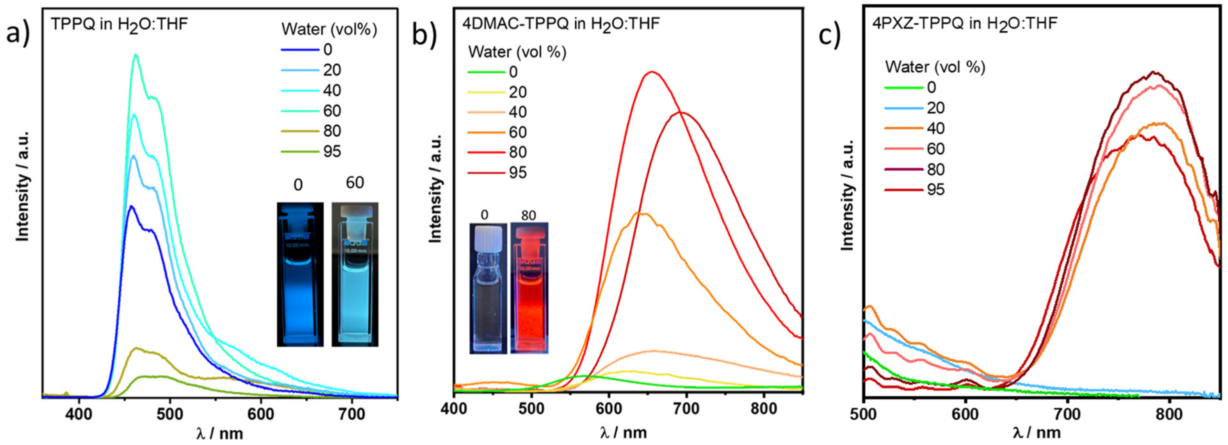

Fig. 5 (a) PL spectra of **TPPQ** (5×10^{-5} M), (b) **4DMAC-TPPQ** (5×10^{-5} M) and (c) **4PXZ-TPPQ** (5×10^{-5} M) in THF–water mixtures with different water fractions in THF:H_2O at 298 K (λ_{exc} = 315 nm). Inset: photos of photoexcited solutions in different solvent systems as mentioned in the figures.

crystalline aggregates in THF/H_2O solution (f_w = 80%), we measured the PL spectra of the dried aggregates isolated from the THF/H_2O solution. These spectra closely resemble those of the neat films of **TPPQ**, **4DMAC-TPPQ** and **4PXZ-TPPQ** (Fig. S30, ESI†), indicating that the excited-state species are likely the same for both types of samples.

Photophysical studies in thin films

We next focused our attention on the photophysical properties of **TPPQ**, **4DMAC-TPPQ** and **4PXZ-TPPQ** doped in poly(methylmethacrylate) (PMMA) and in 4,4′-bis(*N*-carbazolyl)-1,1′-biphenyl (CBP) and in neat thin films. Initially, we measured the photophysical properties of the three emitters as 10 wt% doped films in PMMA as the polarity of this host closely mimics that of toluene. The absorption bands of all three compounds are of similar energy to those in toluene, with the weak CT band observed in the range of 451–650 nm for **4DMAC-TPPQ** while it is more red-shifted for **4PXZ-TPPQ** (Fig. S31a, ESI†). Upon photoexcitation at 315 nm, **TPPQ** shows a structured emission profile at 466 nm (Φ_{PL} = 4.7%), similar to that measured in toluene, while the CT-based unstructured emission is at 635 nm for **4DMAC-TPPQ** (Φ_{PL} = 14.3%) and at 681 nm for **4PXZ-TPPQ** (Φ_{PL} = 3.0%), emission that is blue-shifted by 15 and 81 nm, respectively, compared to the λ_{PL} in toluene (Fig. S31b, ESI†). The emission of **TPPQ** decays with bi-exponential kinetics, with an average lifetime, τ_{PL}, of 2.1 ns. The time-resolved PL of **4DMAC-TPPQ** and **4PXZ-TPPQ** shows multiexponential decay kinetics, with average prompt lifetimes, τ_p, of 25.2 and 15.8 ns, respectively (Fig. S32, ESI†), and average delayed lifetimes, τ_d, of 390.9 and 342.5 μs, respectively (Fig. S33 and Table S8, ESI†). The contribution from the delayed emission increases with increasing temperature, indicating that its origin is TADF.

To best evaluate whether these compounds could act as promising emitters in red-to-NIR OLEDs, we next turned our attention to assessing the photophysics of these three compounds in an OLED-relevant host, CBP, as this host matrix has a sufficiently high triplet energy (T_1 = 2.6 eV) to confine excitons onto the emitters.[38] The λ_{PL} of the 10 wt% doped film of **TPPQ** in CBP is 548 nm and the PL spectrum is much broader (FWHM = 100 nm) and around 80 nm bathochromically shifted compared to that in PMMA (λ_{PL} = 466 nm) and in solutions (λ_{PL} = 456 nm) (Fig. 6). There is only a small red-shift (only 10 nm) of the λ_{PL} and moderate decrease in the Φ_{PL} upon increasing the doping concentration of **TPPQ** from 5 to 30 wt% in CBP (Fig. S34a and Table S10, ESI†). To understand the large red-shift in the emission band of **TPPQ** in CBP in comparison to both in solution and in PMMA, we checked the PL spectrum of **TPPQ** in another host, 2,2′,2″-(1,3,5-benzinetriyl)-tris(1-phenyl-1*H*-benzimidazole) (TPBi), Fig. S34a (ESI†). The 5 wt% doped films of **TPPQ** in TBPi emits at λ_{PL} of 470 nm and has a Φ_{PL} of 4.8%, which is very similar to the properties in toluene and in the 10 wt% doped film in PMMA. Notably, the remarkably red-shifted emission of the 10 wt% doped film of **TPPQ** in CBP is reminiscent of the emission profile after UV exposure in

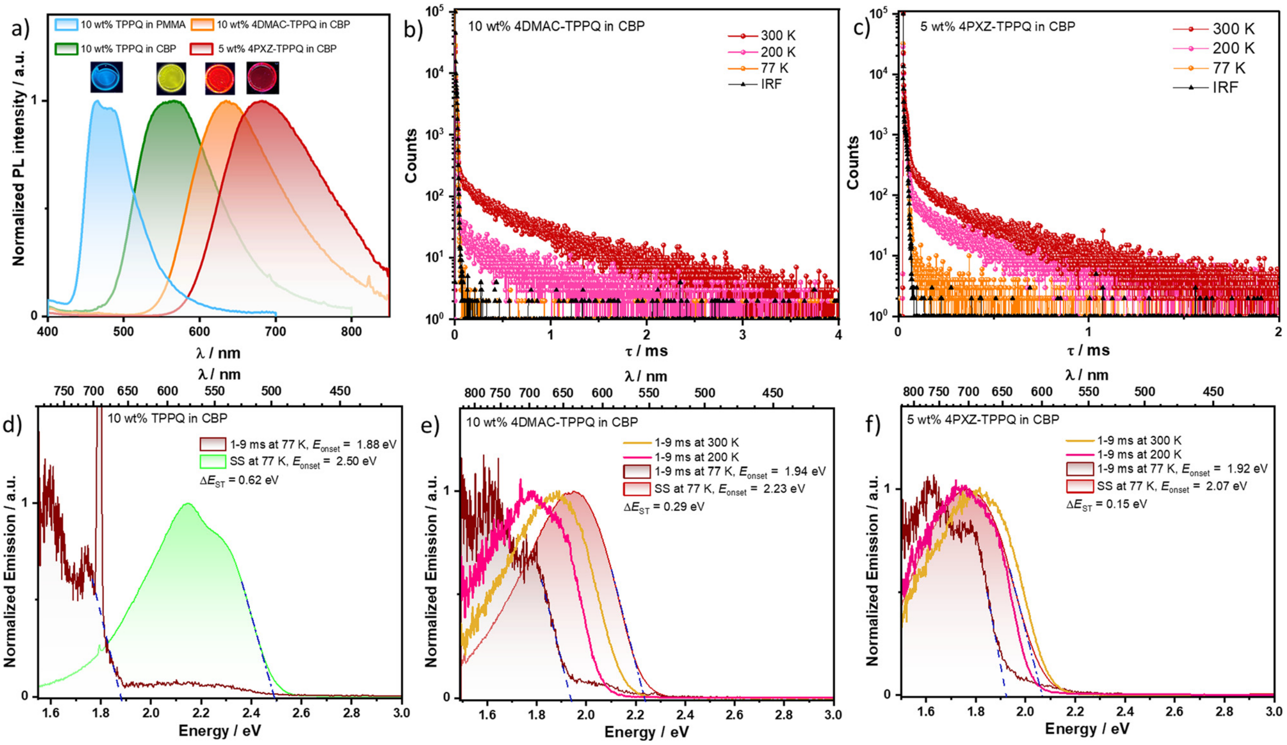

Fig. 6 (a) Photoluminescence spectra of the 10 wt% doped film of **TPPQ** in PMMA and the 10 wt% **4DMAC-TPPQ** and 5 wt% **4PXZ-TPPQ** doped films in CBP at 295 K (λ_{exc} = 340 nm). Inset: photos of photoexcited thin films; (b) and (c) temperature-dependent time-resolved PL decay (λ_{exc} = 340 nm) of 10 wt% **4DMAC-TPPQ** and 5 wt% **4PXZ-TPPQ** doped films in CBP; (d)–(f) steady-state fluorescence at 77 K and phosphorescence spectra (acquisition time range of 1–9 ms) at 300, 200 and 77 K of 10 wt% **TPPQ**, 10 wt% **4DMAC-TPPQ** and 5 wt% **4PXZ-TPPQ** doped films in CBP (λ_{exc} = 340 nm).

ethereal solvents (*vide supra*). This may imply that there is an exciplex between CBP and **TPPQ** that emits at a similar energy to the **TPPQ** excimer. The photophysical properties of the doped films (5–50 wt%) of **4DMAC-TPPQ** and **4PXZ-TPPQ** in CBP and the neat films are shown in Fig. S34b, c and S35–S40 (ESI†) and Table 2. Of these films, the highest Φ_{PL} was found to be 21.0% for **4DMAC-TPPQ** and 10.0% for **4PXZ-TPPQ** as 10 and 5 wt% doped films in CBP, respectively. The λ_{PL} of the 10 wt% doped film of **4DMAC-TPPQ** in CBP is 635 nm, which is very similar to that of the 10 wt% doped film in PMMA (Fig. 6 and Fig. S31, ESI†). The emission for this compound does not significantly change across a doping range from 5–50 wt% and even as the neat film (λ_{PL} ranging from 627 to 654 nm, Fig. S34b, ESI† and Table 2). The λ_{PL} of **4PXZ-TPPQ** is significantly shifted to the NIR region compared to that of **4DMAC-TPPQ**, at 682 nm for the 5 wt% doped film, at 713 nm for the 50 wt% doped film, and 770 nm for the neat film (Fig. S34c, ESI†). The substantially red-shifted emission as a function of doping concentration of **4PXZ-TPPQ** in comparison to **4DMAC-TPPQ** may be attributed to the formation of aggregates in the former resulting in strong interactions between adjacent chromophores. The emission profile of the neat films of **4DMAC-TPPQ** and **4PXZ-TPPQ** match well those in THF:H_2O (f_w = 80%), indicating that the species responsible for the emission in each is the excimer.

At 77 K, the λ_{PL} of the steady-state PL spectrum of the 10 wt% doped film of **TPPQ** in CBP is 578 nm, while the delayed emission spectrum peaks at a λ_{Ph} of 775 nm (Fig. 6). The corresponding S_1 and T_1 energies are 2.50 and 1.88 eV, thus the ΔE_{ST} is 0.62 eV. The phosphorescence of **TPPQ** in CBP closely resembles that in glassy MCH, indicating that it occurs from the same ^{3}LE state. The S_1 and T_1 energies of the 10 wt% doped film of **4DMAC-TPPQ** in CBP are 2.23 and 1.94 eV, while those of the 5 wt% doped film of **4PXZ-TPPQ** in CBP are 2.07 and 1.92 eV (Fig. 6). The corresponding ΔE_{ST} for **4DMAC-TPPQ** is 0.29 eV, and 0.15 eV for **4PXZ-TPPQ**. Given that the T_1 state energy remains effectively the same for the same LE state, the smaller ΔE_{ST} values for the three emitters in CBP are due to the stabilization of the S_1 state. In comparison to the doped film (5 wt%), the S_1 energy of the neat film of **4PXZ-TPPQ** is significantly red shifted at 1.85 eV (ΔS_1 = 0.25 eV), while the neat film of **4DMAC-TPPQ** showed a small red-shift at 2.12 eV (ΔS_1 = 0.11 eV) in comparison to the doped film of 10 wt% **4DMAC-TPPQ** in CBP, however, the T_1 energies of the neat films of both emitters are similarly red-shifted. The ΔE_{ST} of neat **4PXZ-TPPQ** is significantly smaller at 0.04 eV, while ΔE_{ST} of neat **4DMAC-TPPQ** is the same as the doped film, at 0.29 eV (Fig. S38, S40, ESI† and Table 2). These large declines in S_1 energy and ΔE_{ST} of the neat film **4PXZ-TPPQ** in comparison to doped films could be explained by the synergistic effect of the transformation of exciton states due to the formation of aggregates and shortening intermolecular distance because of planar phenoxazine motifs, which induce π–π interactions between adjacent molecules in neat film **4PXZ-TPPQ** compared with the doped film.[21]

As expected, no delayed emission was observed in the 10 wt% doped film of **TPPQ** in CBP and the emission decays with biexponential kinetics, with an average lifetime, τ_{PL} of 42.8 ns at 300 K. In contrast, the 10 wt% doped film of **4DMAC-TPPQ** and 5 wt% doped film of **4PXZ-TPPQ** in CBP show multi-exponential decay kinetics, with an average prompt lifetime, τ_p of 25.2 and 17.6 ns, while the average delayed lifetime (τ_d) is 564.5 and 303.9 μs at a λ_{PL} of 635 and 680 nm, respectively at 300 K (Fig. 6b and c). The corresponding estimated k_{RISC} and k_{ISC} of the 10 wt% **4DMAC-TPPQ** in CBP is 1.32×10^3 and 2.00×10^7 s^{-1} which slightly increase to 2.48×10^3 and 3.17×10^7 s^{-1} for the 5 wt% doped **4PXZ-TPPQ** in CBP, respectively (Table 2). On the other hand, the τ_p of the neat film of **4DMAC-TPPQ** is 27.2 ns and the τ_d is 109.4 μs, while the τ_p and τ_d for the neat film of **4PXZ-TPPQ** are much shorter at 3.7 ns and 2.05 μs, respectively. Therefore, the k_{RISC} of the neat film of **4PXZ-TPPQ** significantly increased (4.9×10^5 s^{-1}) in comparison to the neat film of **4DMAC-TPPQ** (5.03×10^3 s^{-1}) which is strongly aligned with the reduced ΔE_{ST} of neat **4PXZ-TPPQ**.

Table 2 Photophysical properties of **TPPQ**, **4DMAC-TPPQ** and **4PXZ-TPPQ** in the CBP host

Doping/wt%	$\lambda_{PL}{}^c$/nm	$\Phi_{PL}{}^d$/%	$E_{S_1}{}^e$/eV	$E_{T_1}{}^e$/eV	$\Delta E_{ST}{}^f$/eV	$\tau_p{}^g$/ns	$\tau_d{}^h$/μs	$k_{RISC}{}^i$/s^{-1} ($\times 10^3$)	$k_{ISC}{}^i$/s^{-1} ($\times 10^7$)	$k_{s,nr}{}^i$/s^{-1} ($\times 10^7$)	$k_{s,r}{}^i$/s^{-1} ($\times 10^6$)
					TPPQ						
10[a]	548	8.8 (8.5)	2.50	1.88	0.62	42.8	—	—	—	—	—
					4DMAC-TPPQ						
10[a]	635	21.0 (17.2)	2.23	1.94	0.29	25.2	564.5	1.32 ± 0.8	2.00 ± 1.3	2.6	6.8
100[a]	654	4.3 (4.1)	2.12	1.83	0.29	27.2	109.4	5.03 ± 4.5	1.85 ± 1.7	3.3	1.5
					4PXZ-TPPQ						
5[a]	682	10.2 (8.2)	2.09	1.94	0.15	17.6	303.9	2.48 ± 1.6	3.17 ± 2.1	4.1	4.7
100[b]	770	1.5 (1.0)	1.85	1.81	0.04	3.7	2.05[g]	489 ± 243	17.7 ± 8.8	17.6	2.7

[a] Spin-coated film and annealed at 55 °C for 1 minute. [b] Drop-cast film and annealed at 70 °C for 1 minute. [c] PL measured under vacuum, λ_{exc} = 340 nm for all films except 100 wt% **4PXZ-TPPQ**, which has λ_{exc} = 465 nm. [d] Photoluminescence quantum yield (Φ_{PL}) of thin films determined using an integrating sphere (λ_{exc} = 305 nm or 340 nm) under a N_2 atmosphere at 298 K. The values in parentheses are in the presence of O_2 at 298 K. [e] E_{S_1} and E_{T_1} were obtained from the onset of the steady-state and phosphorescence spectra (time window: 1–9 ms), respectively, of doped films in CBP at 77 K, λ_{exc} = 340 nm, and for 100 wt% **4PXZ-TPPQ**, λ_{exc} = 465 nm. [f] $\Delta E_{ST} = E_{S_1} - E_{T_1}$. [g] Prompt lifetime was measured by TCSPC, λ_{exc} = 375 nm, the average lifetimes were calculated by using the equation $\tau_{avg} = \Sigma A_i \tau_i^2 / \Sigma A_i \tau_i$, (where A_i is the pre-exponential for lifetime τ_i). [h] Delayed emission was measured by MCS, using a microsecond flash lamp as an excitation source, λ_{exc} = 340 nm. [i] $k_{s,nr}$, $k_{s,r}$, k_{RISC} and k_{ISC} were calculated according to the method given in ref. 39 and 40.

The temperature-dependent time-resolved PL decay studies of both emitters indicate that these compounds are TADF active not only in doped films but also as their aggregates (Fig. S38 and S40, ESI†).

We next measured the delayed emission spectrum as a function of temperature of the respective 10 and 5 wt% films of **4DMAC-TPPQ** and **4PXZ-TPPQ** in CBP (Fig. 6e, f and Table S10, ESI†). There is an apparent shifting of the delayed emission, attributed to phosphorescence, as a function of temperature. The T_1 state of **4DMAC-TPPQ** red-shifts from 2.15 eV at 300 K to 2.06 eV at 200 K to 1.94 eV at 77 K (Fig. 6e and Table S10, ESI†). Similarly, the T_1 state of **4PXZ-TPPQ** red-shifts from 2.10 eV at 300 K to 2.02 eV at 200 K and 1.92 eV at 77 K (Fig. 6f and Table S10, ESI†). The apparent blue-shift of triplet states from 77 to 300 K in both molecules could be due to the fact that at 300 K the delayed emission originates from the monomer while at 77 K the delayed emission comes from the aggregate. This is supported by the TDA-DFT calculations (*vide supra*).

OLED characterization

Having identified CBP as a viable host, we next proceeded to fabricate solution-processed OLEDs (SP-OLEDs) with **4DMAC-TPPQ** and **4PXZ-TPPQ**; furthermore, recognizing the AIE properties of these emitters, we also explored SP-OLEDs using neat films of both emitters. We employed a bottom-emitting OLED

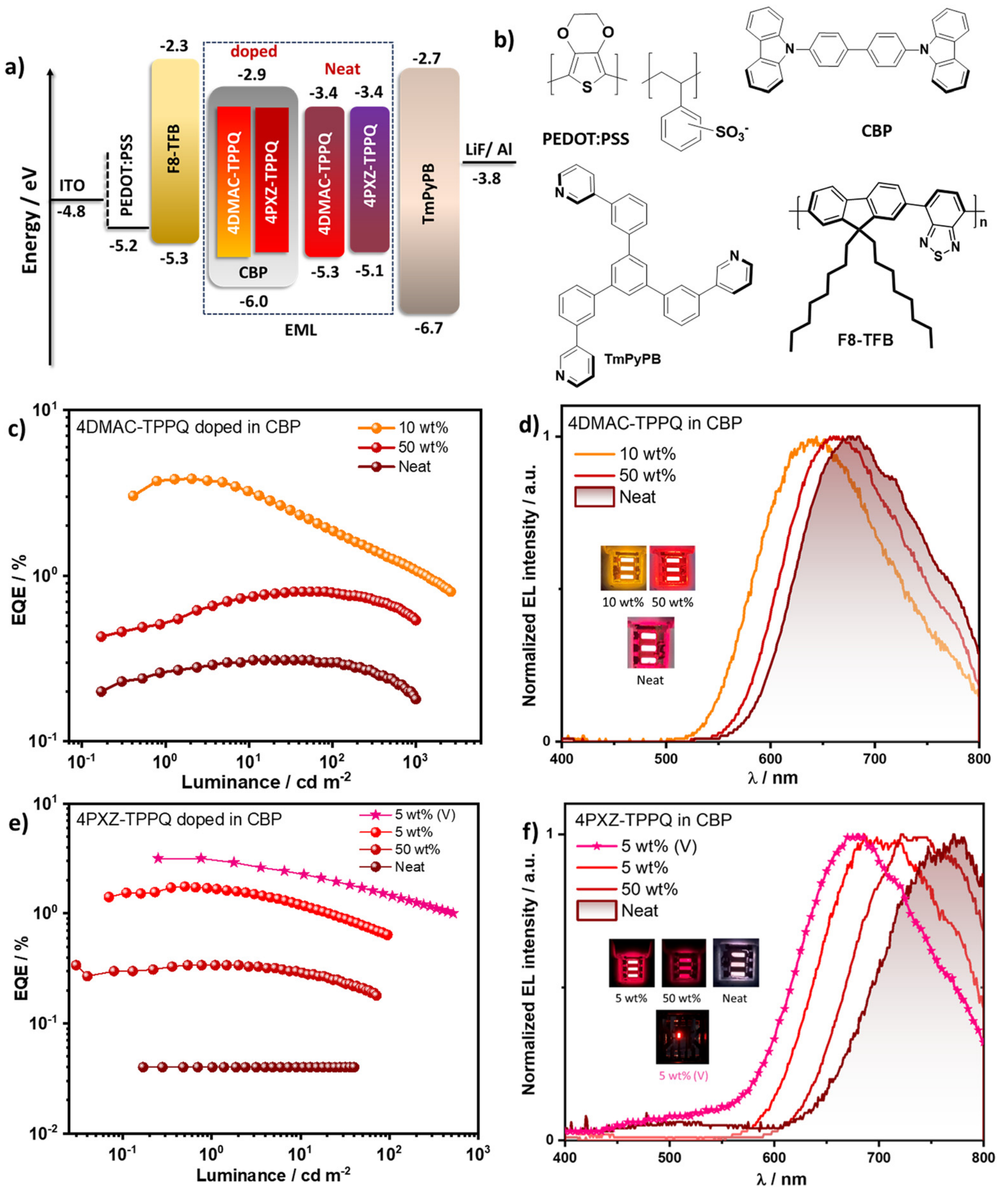

Fig. 7 (a) Energy level diagram of materials employed in the devices; (b) molecular structure of materials used in the devices; (c) external quantum efficiency *versus* luminance curves and (d) electroluminescence spectra of the SP-OLEDs of **4DMAC-TPPQ** (10 and 50 wt% doped in CBP and neat film); (e) external quantum efficiency *versus* luminance curves and (f) electroluminescence spectra of the SP-OLEDs of **4PXZ-TPPQ** [(10 and 50 wt% doped in CBP and neat film) and (5 wt% doped in CBP: vacuum-deposited OLEDs, V-OLEDs)].

Table 3 Electroluminescence data for the devices

Doping/wt%	V_{on}[a]/V	λ_{EL}[b]/nm	EQE[c]/%	EUE[e]/%
		4DMAC-TPPQ		
10	4.2 (5.6)	640	3.9/3.2/1.9	74.2
50	4.4 (6.1)	670	0.8/0.7/0/8	30.2
100	4.0 (5.6)	685	0.3/0.3/—	27.9
		4PXZ-TPPQ		
5	5.2 (8.8)	686	1.7/1.2/0.6	66.7
50	4.4 (8.2)	735	0.3/0.3/0.2	34.3
100	4.6 (7.3)	780	0.04/0.04/—	10.7
5[d]	3.8 (4.8)	681	3.2/2.3/1.4	—

[a] The turn-on voltage at lowest luminance and 10 cd m^{-2} in parenthesis. [b] The electroluminescence maximum recorded at 7 or 8 V. [c] $EQE_{max}/EQE_{10}/EQE_{100}$. [d] Device was fabricated by vacuum deposition. [e] EUE = exciton utilization efficiency, calculated according to the equation: EQE = $\eta_{ext} \times \Phi_{PL}$ of film × EUE × γ, in which η_{ext} = optical outcoupling efficiency, assumed to be 25% for an isotropic film, and γ = charge-balance factor, assumed to be 100%.

device architecture consisting of: indium tin oxide (ITO)/poly(3,4-ethylenedioxy-thiophene):poly(styrenesulfonate) (PEDOT:PSS) (40 nm)/F8-TFB (25 nm)/EML (25 nm for doped and 30 nm for neat film EMLs)/2,3,5-tri[(3-pyridyl)-phen-3-yl]benzene (TmPyPB) (70 nm)/LiF (1 nm)/Al (100 nm) (Fig. S41, ESI†). ITO and Al serve as the anode and cathode, respectively, PEDOT:PSS acts as the hole-transporting layer, F8-TFB acts as the electron-blocking layer (EBL) and hole-transporting layer (HTL), TmPyPB acts as the electron-transporting layer (ETL), and LiF acts as the electron-injection layer by modifying the work function of the aluminum cathode (Fig. 7b). The EQE–luminance curves and electroluminescence spectra (EL) are shown in Fig. 7 and the current density and luminance *versus* voltage are shown in Fig. S42 (ESI†) and the performance of the OLEDs is summarized in Table 3. The EL spectra mirror the corresponding PL spectra. The λ_{EL} of the SP-OLEDs with **4DMAC-TPPQ** ranged from 640 to 670 nm for the 10 and 50 wt% doped film in CBP EMLs, while the neat film SP-OLEDs emitted at an λ_{EL} of 683 nm. As expected, the SP-OLEDs with **4PXZ-TPPQ** emitted further into the NIR, with an λ_{EL} of 686 nm (5 wt% in CBP), 735 nm (50 wt% in CBP), and 780 nm (for neat film devices) (Table 3). Of the devices fabricated with **4DMAC-TPPQ**, the highest EQE_{max} was achieved with 10 wt% doping at 3.9%; the efficiency decreased to 1.9% at 100 cd m^{-2}. The 50 wt% and neat film devices generally exhibited relatively low EQE, with EQE_{max} of 0.8 and 0.3%, respectively (Table 3). The EQE_{max} for the device with 5 wt% **4PXZ-TPPQ** in CBP was 1.7%; the EQE_{max} was 0.3% for the 50 wt% doped device and 0.04% for the neat film OLEDs, values that are consistent with their lower Φ_{PL}. For comparison, we fabricated vacuum-deposited devices (VD-OLEDs) with 5 wt% **4PXZ-TPPQ** in CBP, using the device structure shown in Fig. S41 (ESI†) and Table 3. Notably, the VD-OLEDs performance improved, reflected in the higher EQE_{max} of 3.2% at λ_{EL} at 681 nm, a similar EL spectrum to that observed for the 5 wt% SP-OLEDs. The fabrication of VD-OLEDs was not possible for **4DMAC-TPPQ** because its molecular weight was too high. The turn-on voltages for the SP-OLEDs range from 4.0 to 5.2 V, while that for the VD-OLEDs is decreased at 3.8 V. Furthermore, the exciton utilization efficiency (EUE) of the SP-OLEDs with **4DMAC-TPPQ** and **4PXZ-TPPQ** is high as 74 and 67%, respectively, indicating that there is significant triplet exciton harvesting in these devices. The EL spectrum of the neat film SP-OLED with **4PXZ-TPPQ** mirrors the PL spectrum (λ_{PL} = 770 nm). These devices are, to the best of our knowledge, the reddest of those based on emitters containing quinoxaline acceptors (Fig. S43 and Table S11, ESI†).

Conclusion

We have developed deep-red and NIR TADF emitters containing an extended π-conjugated pyrazine-quinoxaline (**PQ**) acceptor with a particularly deep LUMO at −2.74 eV. The compounds **4DMAC-TPPQ** and **4PXZ-TPPQ** emit at 650 and 762 nm in toluene, which are significantly red-shifted in comparison to the donor-free parent compound **TPPQ** (λ_{PL} = 456 nm). AIE behavior was observed in THF:water mixtures of all compounds. While **TPPQ** is fluorescent, both **4DMAC-TPPQ** and **4PXZ-TPPQ** exhibit TADF as both doped films in CBP and as neat films. The 10 wt% doped film of **4DMAC-TPPQ** in CBP emits at 635 nm and the ΔE_{ST} is 0.29 eV, while the neat film emits at 654 nm yet has the same ΔE_{ST}. On the other hand, the 5 wt% doped film of **4PXZ-TPPQ** in CBP emits at 682 nm and the ΔE_{ST} is 0.15 eV, while the neat film emits at 770 nm and the ΔE_{ST} is much smaller at 0.04 eV. The undoped solution-processed OLEDs (SP-OLEDs) with **4DMAC-TPPQ** and **4PXZ-TPPQ** are particularly remarkable, emitting at 685 and 780 nm and exhibiting EQE_{max} of 0.3 and 0.04%, respectively.

Data availability

The research data supporting this publication can be accessed at **https://doi.org/10.17630/63338f36-6958-437d-acb2-447a2ff03f96**.

Conflicts of interest

There are no conflicts to declare.

Acknowledgements

AKG is grateful to the Royal Society for a Newton International Fellowship NF171163. We acknowledge support from the Engineering and Physical Sciences Research Council of the UK (grants EP/W007517/1, EP/P010482/1, and EP/L017008/1). We are also grateful for financial support from the University of St Andrews Restarting Research and Restarting Interdisciplinary Research Funding Schemes (SARRF and SARIRF) which are funded through the Scottish Funding Council grant reference SFC/AN/08/020. This project has received funding from the European Union's Horizon 2020 research and innovation programme under the Marie Sklodowska-Curie grant agreement no. 101025143 (TADF-DLC-OLEDs). The authors thank

Dr Tomas Matulaitis for helpful discussions and Dr Gavin Peters for TGA/DSC measurements.

References

1 S. Wang, J. Liu, G. Feng, L. G. Ng and B. Liu, NIR-II Excitable Conjugated Polymer Dots with Bright NIR-I Emission for Deep In Vivo Two-Photon Brain Imaging Through Intact Skull, *Adv. Funct. Mater.*, 2019, **29**, 1808365, DOI: **10.1002/adfm.201808365**.

2 A. T. Eggebrecht, S. L. Ferradal, A. Robichaux-Viehoever, M. S. Hassanpour, H. Dehghani, A. Z. Snyder, T. Hershey and J. P. Culver, Mapping distributed brain function and networks with diffuse optical tomography, *Nat. Photonics*, 2014, **8**, 448–454, DOI: **10.1038/nphoton.2014.107**.

3 Q. He, M. Wang, L. Zhao, B. Xu, W. Tian and L. Zhang, Near-infrared aggregation-induced emission materials: Bibliometric analysis and their application in biomedical field, *Aggregate*, 2024, **5**, e505, DOI: **10.1002/agt2.505**.

4 R. Singh, A. K. Gupta and C. P. Pradeep, Synthesis of a New Series of Organic Solid-State Near-Infrared Emitters: The Role of Crystal Packing and Weak Intermolecular Interactions and Application in Latent Fingerprint Detection, *Cryst. Growth Des.*, 2021, **21**, 1062–1076, DOI: **10.1021/acs.cgd.0c01392**.

5 M. Kono, H. Ueki and S.-I. Umemura, Near-infrared finger vein patterns for personal identification, *Appl. Opt.*, 2002, **41**, 7429–7436, DOI: **10.1364/AO.41.007429**.

6 Z. Lan, Y. Lei, W. K. E. Chan, S. Chen, D. Luo and F. Zhu, Near-infrared and visible light dual-mode organic photodetectors, *Sci. Adv.*, 2020, **6**, eaaw8065, DOI: **10.1126/sciadv.aaw8065**.

7 C. Si, A. K. Gupta, B. Basumatary, A. P. McKay, D. B. Cordes, A. M. Z. Slawin, I. D. W. Samuel and E. Zysman-Colman, Multi-Responsive Thermally Activated Delayed Fluorescence Materials: Optical $ZnCl_2$ Sensors and Efficient Green to Deep-Red OLEDs, *Adv. Funct. Mater.*, 2024, **34**, 2315935, DOI: **10.1002/adfm.202315935**.

8 X. Zhao, C. Yao, T. Liu, J. C. Hamill Jr., G. O. Ngongang Ndjawa, G. Cheng, N. Yao, H. Meng and Y.-L. Loo, Extending the Photovoltaic Response of Perovskite Solar Cells into the Near-Infrared with a Narrow-Bandgap Organic Semiconductor, *Adv. Mater.*, 2019, **31**, 1904494, DOI: **10.1002/adma.201904494**.

9 B. Xu, C. Jin, J.-S. Park, H. Liu, X. Lin, J. Cui, D. Chen and J. Qiu, Emerging near-infrared luminescent materials for next-generation broadband optical communications, *InfoMat*, 2024, **6**, e12550, DOI: **10.1002/inf2.12550**.

10 J.-C. G. Bünzli and S. V. Eliseeva, Lanthanide NIR luminescence for telecommunications, bioanalyses and solar energy conversion, *J. Rare Earths*, 2010, **28**, 824–842, DOI: **10.1016/S1002-0721(09)60208-8**.

11 H. Q. Ye, Z. Li, Y. Peng, C. C. Wang, T. Y. Li, Y. X. Zheng, A. Sapelkin, G. Adamopoulos, I. Hernández, P. B. Wyatt and W. P. Gillin, Organo-erbium systems for optical amplification at telecommunications wavelengths, *Nat. Mater.*, 2014, **13**, 382–386, DOI: **10.1038/nmat3910**.

12 K. Tuong Ly, R.-W. Chen-Cheng, H.-W. Lin, Y.-J. Shiau, S.-H. Liu, P.-T. Chou, C.-S. Tsao, Y.-C. Huang and Y. Chi, Near-infrared organic light-emitting diodes with very high external quantum efficiency and radiance, *Nat. Photonics*, 2017, **11**, 63–68, DOI: **10.1038/nphoton.2016.230**.

13 R. Nagata, H. Nakanotani and C. Adachi, Near-Infrared Electrophosphorescence up to 1.1 μm using a Thermally Activated Delayed Fluorescence Molecule as Triplet Sensitizer, *Adv. Mater.*, 2017, **29**, 1604265, DOI: **10.1002/adma.201604265**.

14 A. Zampetti, A. Minotto, B. M. Squeo, V. G. Gregoriou, S. Allard, U. Scherf, C. L. Chochos and F. Cacialli, Highly Efficient Solid-State Near-infrared Organic Light-Emitting Diodes incorporating A–D–A Dyes based on α,β-unsubstituted "BODIPY" Moieties, *Sci. Rep.*, 2017, **7**, 1611, DOI: **10.1038/s41598-017-01785-2**.

15 Y. Xiao, H. Wang, Z. Xie, M. Shen, R. Huang, Y. Miao, G. Liu, T. Yu and W. Huang, NIR TADF emitters and OLEDs: challenges, progress, and perspectives, *Chem. Sci.*, 2022, **13**, 8906–8923, DOI: **10.1039/d2sc02201j**.

16 H. U. Kim, T. Kim, C. Kim, M. Kim and T. Park, Recent Advances in Structural Design of Efficient Near-Infrared Light-Emitting Organic Small Molecules, *Adv. Funct. Mater.*, 2023, **33**, 2208082, DOI: **10.1002/adfm.202208082**.

17 A. K. Gupta, A. Kumar, R. Singh, M. Devi, A. Dhir and C. P. Pradeep, Facile Synthesis of an Organic Solid State Near-Infrared-Emitter with Large Stokes Shift via Excited-State Intramolecular Proton Transfer, *ACS Omega*, 2018, **3**, 14341–14348, DOI: **10.1021/acsomega.8b02116**.

18 H. Uoyama, K. Goushi, K. Shizu, H. Nomura and C. Adachi, Highly efficient organic light-emitting diodes from delayed fluorescence, *Nature*, 2012, **492**, 234–238, DOI: **10.1038/nature11687**.

19 J. M. Dos Santos, D. Hall, B. Basumatary, M. Bryden, D. Chen, P. Choudhary, T. Comerford, E. Crovini, A. Danos, J. De, S. Diesing, M. Fatahi, M. Griffin, A. K. Gupta, H. Hafeez, L. Hämmerling, E. Hanover, J. Haug, T. Heil, D. Karthik, S. Kumar, O. Lee, H. Li, F. Lucas, C. F. R. Mackenzie, A. Mariko, T. Matulaitis, F. Millward, Y. Olivier, Q. Qi, I. D. W. Samuel, N. Sharma, C. Si, L. Spierling, P. Sudhakar, D. Sun, E. Tankelevičiūtė, M. Duarte Tonet, J. Wang, T. Wang, S. Wu, Y. Xu, L. Zhang and E. Zysman-Colman, The Golden Age of Thermally Activated Delayed Fluorescence Materials: Design and Exploitation, *Chem. Rev.*, 2024, **124**, 13736–14110, DOI: **10.1021/acs.chemrev.3c00755**.

20 Z. Zhao, H. Zhang, J. W. Y. Lam and B. Z. Tang, Aggregation-Induced Emission: New Vistas at the Aggregate Level, *Angew. Chem., Int. Ed.*, 2020, **59**, 9888–9907, DOI: **10.1002/anie.201916729**.

21 J. Xue, Q. Liang, R. Wang, J. Hou, W. Li, Q. Peng, Z. Shuai and J. Qiao, Highly Efficient Thermally Activated Delayed Fluorescence via J-Aggregates with Strong Intermolecular Charge Transfer, *Adv. Mater.*, 2019, **31**, 1808242, DOI: **10.1002/adma.201808242**.

22 Z. Hu, L. Feng and P. Yang, 2,1,3-Benzothiadiazole Deriva tive Small Molecule Fluorophores for NIR-II Bioimaging, *Adv. Funct. Mater.*, 2024, **34**, 2310818, DOI: **10.1002/adfm.202310818**.

23 Y. Liu, Z. Deng, J. Li, J. Xie, X. Feng, Z. Qiu, G. Xie, Z. Zhao and B. Z. Tang, Deep-red/NIR AIEgens based on electron-withdrawing dithiafulvalene-fused benzothiadiazole for solution-processed non-doped OLEDs, *Mater. Chem. Front.*, 2023, **7**, 5431–5438, DOI: 10.1039/d3qm00598d.

24 J. Jiang, Z. Xu, J. Zhou, M. Hanif, Q. Jiang, D. Hu, R. Zhao, C. Wang, L. Liu, D. Ma, Y. Ma and Y. Cao, Enhanced Pi Conjugation and Donor/Acceptor Interactions in D–A–D Type Emitter for Highly Efficient Near-Infrared Organic Light-Emitting Diodes with an Emission Peak at 840 nm, *Chem. Mater.*, 2019, **31**, 6499–6505, DOI: 10.1021/acs.chemmater.8b04894.

25 T. Liu, L. Zhu, C. Zhong, G. Xie, S. Gong, J. Fang, D. Ma and C. Yang, Naphthothiadiazole-Based Near-Infrared Emitter with a Photoluminescence Quantum Yield of 60% in Neat Film and External Quantum Efficiencies of up to 3.9% in Nondoped OLEDs, *Adv. Funct. Mater.*, 2017, **27**, 1606384, DOI: 10.1002/adfm.201606384.

26 G. Hong, C. Si, A. K. Gupta, C. Bizzarri, M. Nieger, I. D. W. Samuel, E. Zysman-Colman and S. Bräse, Fluorinated dibenzo[*a*,*c*]-phenazine-based green to red thermally activated delayed fluorescent OLED emitters, *J. Mater. Chem. C*, 2022, **10**, 4757–4766, DOI: 10.1039/d1tc04918f.

27 T. Huang, D. Liu, J. Jiang and W. Jiang, Quinoxaline and Pyrido[*x*,*y*-*b*]pyrazine-Based Emitters: Tuning Normal Fluorescence to Thermally Activated Delayed Fluorescence and Emitting Color over the Entire Visible-Light Range, *Chem. – Eur. J.*, 2019, **25**, 10926–10937, DOI: 10.1002/chem.201902116.

28 V. K. Vishwakarma, V. Adupa, K. Anki Reddy and A. Ammathnadu Sudhakar, Experimental and theoretical investigations of acid sensing properties of pyrazino[2,3-*g*]quinoxaline derivatives, *J. Mol. Struct.*, 2021, **1225**, 129120, DOI: 10.1016/j.molstruc.2020.129120.

29 A. Shah, V. K. Vishwakarma, N. Lhouvum, A. A. Sudhakar, P. Kumar, A. K. Srivastava, F. Dubois, T. Chomchok, N. Chattham and D. P. Singh, Pyrazino[2,3-*g*]quinoxaline core-based organic liquid crystalline semiconductor: Proficient hole transporting material for optoelectronic devices, *J. Mol. Liq.*, 2024, **393**, 123535, DOI: 10.1016/j.molliq.2023.123535.

30 V. K. Vishwakarma, S. Nath, M. Gupta, D. K. Dubey, S. S. Swayamprabha, J.-H. Jou, S. K. Pal and A. A. Sudhakar, Room-Temperature Columnar Liquid Crystalline Materials Based on Pyrazino[2,3-*g*]quinoxaline for Bright Green Organic Light-Emitting Diodes, *ACS Appl. Electron. Mater.*, 2019, **1**, 1959–1969, DOI: 10.1021/acsaelm.9b00477.

31 X. Wang, Y. Zhou, T. Lei, N. Hu, E.-Q. Chen and J. Pei, Structural–Property Relationship in Pyrazino[2,3-*g*]quinoxaline Derivatives: Morphology, Photophysical, and Waveguide Properties, *Chem. Mater.*, 2010, **22**, 3735–3745, DOI: 10.1021/cm100798q.

32 M. Chen, X. Hu, J. Liu, B. Li, N. L. C. Leung, L. Viglianti, T. S. Cheung, H. H. Y. Sung, R. T. K. Kwok, I. D. Williams, A. Qin, J. W. Y. Lam and B. Z. Tang, Rational design of red AIEgens with a new core structure from non-emissive heteroaromatics, *Chem. Sci.*, 2018, **9**, 7829–7834, DOI: 10.1039/c8sc02810a.

33 A. K. Gupta, W. Li, A. Ruseckas, C. Lian, C. L. Carpenter-Warren, D. B. Cordes, A. M. Z. Slawin, D. Jacquemin, I. D. W. Samuel and E. Zysman-Colman, Thermally Activated Delayed Fluorescence Emitters with Intramolecular Proton Transfer for High Luminance Solution-Processed Organic Light-Emitting Diodes, *ACS Appl. Mater. Interfaces*, 2021, **13**, 15459–15474, DOI: 10.1021/acsami.1c02248.

34 A. K. Gupta, T. Matulaitis, D. B. Cordes, A. M. Z. Slawin, I. D. W. Samuel and E. Zysman-Colman, Highly twisted α-diketone-based thermally activated delayed fluorescence emitters and their use in organic light-emitting diodes, *Can. J. Chem.*, 2022, **100**, 224–233, DOI: 10.1139/cjc-2021-0208.

35 S. Li, T. Cheng, C. Yin, S. Zhou, Q. Fan, W. Wu and X. Jiang, Phenothiazine *versus* Phenoxazine: Structural Effects on the Photophysical Properties of NIR-II AIE Fluorophores, *ACS Appl. Mater. Interfaces*, 2020, **12**, 43466–43473, DOI: 10.1021/acsami.0c12773.

36 N. G. Connelly and W. E. Geiger, Chemical Redox Agents for Organometallic Chemistry, *Chem. Rev.*, 1996, **96**, 877–910, DOI: 10.1021/cr940053x.

37 C. M. Cardona, W. Li, A. E. Kaifer, D. Stockdale and G. C. Bazan, Electrochemical Considerations for Determining Absolute Frontier Orbital Energy Levels of Conjugated Polymers for Solar Cell Applications, *Adv. Mater.*, 2011, **23**, 2367–2371, DOI: 10.1002/adma.201004554.

38 M. A. Baldo and S. R. Forrest, Transient analysis of organic electrophosphorescence: I. Transient analysis of triplet energy transfer, *Phys. Rev. B: Condens. Matter Mater. Phys.*, 2000, **62**, 10958–10966, DOI: 10.1103/PhysRevB.62.10958.

39 F. B. Dias, T. J. Penfold and A. P. Monkman, Photophysics of thermally activated delayed fluorescence molecules, *Methods Appl. Fluoresc.*, 2017, **5**, 012001, DOI: 10.1088/2050-6120/aa537e.

40 Y. Tsuchiya, S. Diesing, F. Bencheikh, Y. Wada, P. L. dos Santos, H. Kaji, E. Zysman-Colman, I. D. W. Samuel and C. Adachi, Exact Solution of Kinetic Analysis for Thermally Activated Delayed Fluorescence Materials, *J. Phys. Chem. A*, 2021, **125**, 8074–8089, DOI: 10.1021/acs.jpca.1c04056.